



**HAL**  
open science

## **Anisotropic stratification beneath Africa from joint inversion of SKS and P receiver functions**

M. Obrebski, S. Kiselev, L. Vinnik, J. -P. Montagner

► **To cite this version:**

M. Obrebski, S. Kiselev, L. Vinnik, J. -P. Montagner. Anisotropic stratification beneath Africa from joint inversion of SKS and P receiver functions. *Journal of Geophysical Research: Solid Earth*, 2010, 115, 10.1029/2009JB006923 . insu-03605289

**HAL Id: insu-03605289**

**<https://insu.hal.science/insu-03605289>**

Submitted on 11 Mar 2022

**HAL** is a multi-disciplinary open access archive for the deposit and dissemination of scientific research documents, whether they are published or not. The documents may come from teaching and research institutions in France or abroad, or from public or private research centers.

L'archive ouverte pluridisciplinaire **HAL**, est destinée au dépôt et à la diffusion de documents scientifiques de niveau recherche, publiés ou non, émanant des établissements d'enseignement et de recherche français ou étrangers, des laboratoires publics ou privés.

Copyright

## Anisotropic stratification beneath Africa from joint inversion of SKS and P receiver functions

M. Obrebski,<sup>1,2</sup> S. Kiselev,<sup>3</sup> L. Vinnik,<sup>3</sup> and J.-P. Montagner<sup>1</sup>

Received 28 August 2009; revised 6 May 2010; accepted 2 June 2010; published 22 September 2010.

[1] The analysis of rock anisotropy revealed by seismic waves provides fundamental constraints on stress-strain field in the lithosphere and asthenosphere. Nevertheless, the anisotropic models resolved for the crust and the upper mantle using seismic waves sometimes show substantial discrepancies depending on the type of data analyzed. In particular, at several permanent stations located in Africa, previous studies revealed that the observations of SKS splitting are accounted for by models with a single and homogeneous anisotropic layer whereas 3-D tomographic models derived from surface waves exhibit clear anisotropic stratification. Here we tackle the issue of depth-dependent anisotropy by performing joint inversion of receiver functions (RF) and SKS waveforms at four permanent broadband stations along the East African Rift System (EARS) and also on the Congo Craton. For three out of the four stations studied, stratified models allow for the best fit of the data. The vertical variations in the anisotropic pattern show interesting correlations with changes in the thermomechanical state of the mantle associated with the lithosphere-asthenosphere transition and with the presence of hot mantle beneath the Afar region and beneath the EARS branches that surround the Tanzanian Craton. Our interpretation is consistent with the conclusion of earlier studies that suggest that beneath individual stations, multiple sources of anisotropy, chiefly olivine lattice preferred orientation and melt pocket shape preferred orientation in our case, exist at different depths. Our study further emphasizes that multiple layers of anisotropy must often be considered to obtain realistic models of the crust and upper mantle.

**Citation:** Obrebski, M., S. Kiselev, L. Vinnik, and J.-P. Montagner (2010), Anisotropic stratification beneath Africa from joint inversion of SKS and P receiver functions, *J. Geophys. Res.*, 115, B09313, doi:10.1029/2009JB006923.

### 1. Introduction

[2] The region that comprises eastern Africa and southwestern Arabia (Figure 1) hosts a wide variety of past and recent tectonic features. In particular, recent tectonic activity, namely, extensive magmatism (trapps) and continental rifting resumed 30Ma ago. In the Horn of Africa region, the Nubian, Somalian and Arabian plates are connected by three rifts both at continental breakup stage (EARS) and incipient oceanic spreading stage (Aden rift and Red Sea rift). The presence of different kinds of hot spots (Afar, Victoria) in this region has also been suggested. The Afar hot spot probably reflects deep mantle plume activity as suggested by low seismic velocity down to the upper/lower mantle boundary [Ritsema *et al.*, 1999; Debayle *et al.*, 2001; Sebai *et al.*, 2006], magma with large <sup>3</sup>He/<sup>4</sup>He ratio, and high topography. The other east African hot spots may rather result from asthenospheric convective instabilities [Montagner *et al.*, 2007].

[3] Information about the lithospheric strain/stress state and the geometry of asthenospheric flows can be drawn from seismic wave analysis. Indeed, in the crust and upper mantle, the deviatoric stress field causes cracks and melt pockets to open parallel to the maximum compressive stress. As a response to tectonic deformations, seismically anisotropic crystals contained in the crust and mantle rocks also preferentially reorient to accommodate strain. The resulting bulk anisotropy affects the seismic waves that sample a given region in specific way that depends on the characteristics of the local tectonic setting. Such information might help to improve our understanding of several issues specific to eastern Africa such as the structure and the mechanism of the distinct branches of the EARS, the nature of the East African hot spots and the interactions that may exist between all these features.

[4] The previous studies of the anisotropic structure of the lithosphere and asthenosphere beneath Africa have led to contradictory interpretations depending on the approach used, in particular the type of seismic waves analyzed. On one hand, Barruol and Hoffmann [1999], Barruol and Ben Ismail [2001], Ayele *et al.* [2004] and Walker *et al.* [2004] achieved a reasonable fit of SKS splitting observations at several stations around Afar and along the EARS using models with a single homogeneous layer of anisotropy. On the other hand,

<sup>1</sup>Département de Sismologie, Institut de Physique du Globe de Paris, Paris, France.

<sup>2</sup>Now at Seismological Laboratory, Earth and Planetary Science, University of California, Berkeley, California, USA.

<sup>3</sup>Institute of Physics of the Earth, Moscow, Russia.

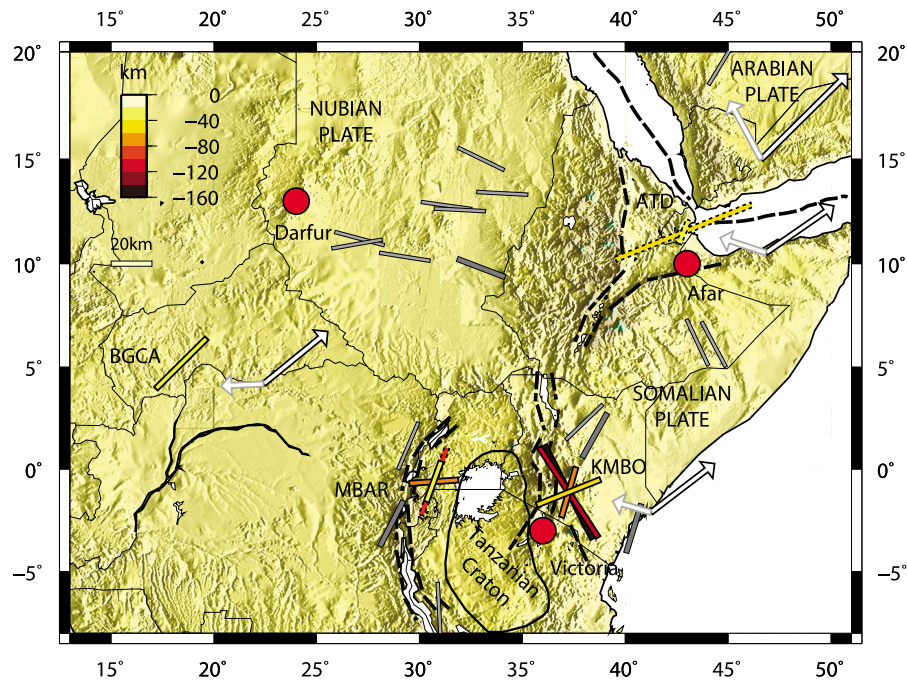


**Figure 1.** Tectonic map of the region under study. The dashed lines indicate the boundaries of the East African Rift System (EARS) and the trend of the oceanic rifts in the Red Sea and in the Aden Gulf. To the south, the EARS splits into a western and an eastern branch that surround the Tanzanian Craton. The red circles are estimates of the position of the Afar, Darfur, and Victoria hot spots. The white arrows indicate the local direction of local absolute plate motion from no net rotation model NUVEL-1 (black contour) and HS3-NUVEL-1A (gray contour). The thick dark grey and thin light grey bars show available A and B quality estimates of the direction of the maximum horizontal compressive stress (MHCS), respectively [Heidbach *et al.*, 2008]. The colored bars at each individual station indicate the direction of the fast axis of propagation in the distinct layers. The color of these bars represents the depth of the top of each layer, and their length is scaled by their thickness (see legend for scale). Only the anisotropic layers that are robustly constrained are shown (see Table 1). A-ranked and B-ranked layers are shown using bars with solid and dashed contours, respectively.

surface wave-based models are suggestive of substantial stratification in the anisotropic structure of the crust and upper mantle [Sebai *et al.*, 2006; Sicilia *et al.*, 2008] in the same region. Surface waves are dispersive and thus provide good depth resolution. Nevertheless, they horizontally average the sampled structures over long distances (500 km for the model of Sicilia *et al.* [2008]). On the contrary, SKS splitting observations yield a typical lateral resolution of a few tens of kilometers but vertically integrate the effect of anisotropy from the core-mantle boundary to the surface. The African continent is made of an assemblage of lithospheric blocks as old as Archean [Begg *et al.*, 2009] and is tectonically active on its eastern edge. Therefore, its lithosphere and asthenosphere are expected to exhibit 3-D heterogeneities with length scale smaller than both the lateral resolution of the surface waves and the vertical resolution of SKS waves. Therefore the models obtained using these two types of waves will be both affected though in a distinct way, which may account for the discrepancies mentioned above.

[5] Finer constraints on the possible stratification of anisotropy beneath Africa can be achieved through simultaneous inversion of several types of data. Here we use receiver functions (RF) and SKS waveforms [Vinnik and Montagner, 1996; Vinnik *et al.*, 2007]. The resolution provided by this method is high not only vertically but also laterally. On

one hand, the RF contain information about the depth of P-to-S conversions produced at velocity discontinuities. On the other hand, the body waves used in our inversion are short periods. At 10s, which is the typical dominant period in our body wave data set, the radius of the first Fresnel zone (the circular area that contains the region sampled around the theoretical raypath) ranges from 30 km at a depth of 50 to 70 km at a depth of 200 km. We applied our joint inversion scheme to the data set of four permanent stations ATD, KMBO, MBAR and BGCA (Figure 1). In three cases, the best fit of the azimuthal variations exhibited by the RF and SKS waves was achieved by using anisotropic models needing vertical stratification of anisotropy.

## 2. Data and Method

[6] The geometry of a given anisotropic structure generates specific azimuthal variations in the seismic waves that can be used as constraints to resolve a 3-D anisotropic model. In an isotropic, horizontally stratified and homogeneous medium, SKS/SKKS waves and P-to-S converted phases are purely radial; that is, all the energy is contained in the Q (or SV) components. The presence of anisotropy causes the SKS phases to split resulting in a nonzero T (or SH) component. P-to-S conversion at a velocity discontinuity involving at

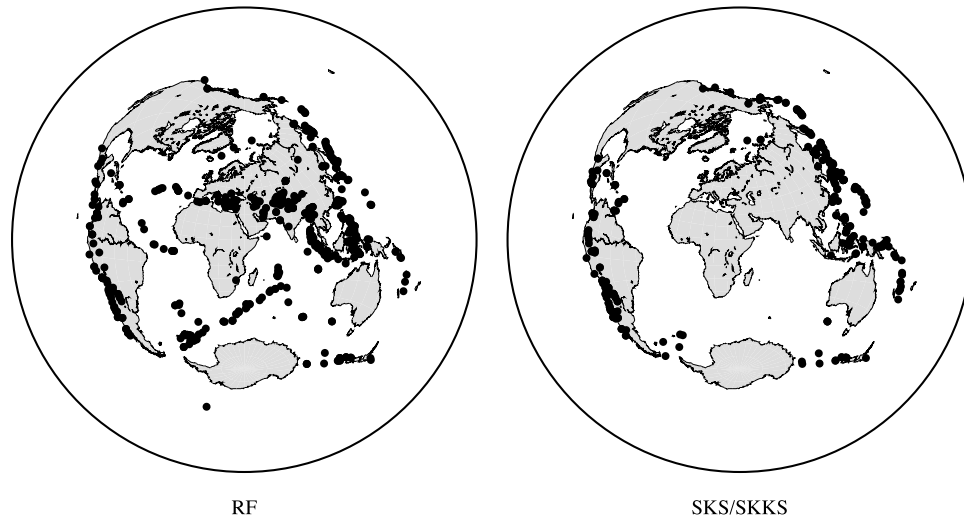


**Figure 2.** Distributions of the earthquakes we used (left) to calculate P receiver functions and (right) to make SKS splitting observations.

least an anisotropic medium leads the converted shear wave to have energy on both the Q and the T component. The way the resulting waveform, polarity and time arrival of these phases varies is a function of the back azimuth of the incoming seismic ray [Keith and Crampin, 1977; Savage, 1998; Levin and Park, 1998]. Nearly homogeneous azimuthal sampling is required to observe properly these variations. Therefore to warrant robust anisotropic models we limited our study to permanent stations, for they have a low intrinsic level of noise and several years of recording. We analyzed the data set of ATD (Arta Tunel, Djibouti, Geoscope, 15 years of data) in the Afar region, KMBO (Kilima Mbogo, Kenya, IRIS/USGS–GSN–GEOFON, 13 years of data) and MBAR (Mbarara, Uganda, IRIS/IDA–GSN, 9 years of data) close to the EARS and BGCA (Bogion, Central African Republic, AFTAC/USGS–GTSN, 8 years of data) on the Congo Craton. The azimuthal coverage achieved in this study is illustrated in Figure 2.

### 2.1. Receiver Functions Preprocessing

[7] Receiver functions were calculated using P and PP waves recorded at epicentral distances between  $30^\circ$  and  $130^\circ$ . Seismograms are low-pass filtered with 0.2 Hz corner frequency, rotated into L (P), Q (SV) and T(SH) directions to separate converted waves from the direct P wave. The L component is then deconvolved from the Q and T component using a time domain deconvolution [Vinnik, 1977]. If several teleseismic waves arrive at a given seismic station broadly from the same direction, they sample a similar region of the receiver side. Therefore, with a view to enhancing the signal-to-noise ratio, individual receiver functions with close back azimuth are stacked into  $20^\circ$  wide azimuthal bins. The number of individual RF in each bin is displayed in Figure 3. We obtained our RF data set using P waves with a wide range of ray parameters. Therefore, the converted and reflected phases that make up the P coda are expected to exhibit some moveout. Nevertheless, using periods larger than 5s as done in this study, this effect is expected to be small in the first 25s of the RF that we use to constrain our models. We visually

inspect all the RF and select only those that are similar to each other before stacking them.

[8] As mentioned above, the anomalous energy observed on the T component of both the SKS and P-to-S conversion may result from several earth complexities, namely, seismic anisotropy, lateral heterogeneities or the presence of a dipping interface between two layers with contrasting velocities. Previous studies showed that the major observable effects of the anisotropy of the upper mantle are captured using a hexagonal symmetry [Savage, 1999; Becker et al., 2006]. Under the assumption of such a symmetric geometry, the seismic waves that sample the medium are affected in a manner that is a periodic function of the azimuth of the ray-path. In particular, if the axis of symmetry is horizontal the signal exhibits strong second (period  $\pi$ ) azimuthal harmonic [Savage, 1998; Levin and Park, 1998]. If the symmetry axis exhibits a substantial dip, the signal also contains a strong first azimuthal harmonic (period  $2\pi$ ). Nevertheless, the second azimuthal harmonic (period  $\pi$ ) remains nonzero [Girardin and Farra, 1998; Vinnik et al., 2007]. The  $\pi$  periodic signature induced by anisotropy can easily be discriminated from that of a medium with small-scale random heterogeneities (not a periodic function of the back azimuth) and also from that of an isotropic stratified medium containing dipping layers ( $2\pi$  periodic with respect to the back azimuth). Using the specific periodicity of the anisotropic signal, the later can be extracted by using a weighted sum of all the individual receiver functions in a way similar to Fourier series. The potential of this *azimuthal filtering* was demonstrated by Girardin and Farra [1998]. Using this approach, we do not assume that earth complexities other than seismic anisotropy (dipping interfaces, heterogeneities) or anisotropy with a more complex symmetry system (orthorhombic) or with a nonhorizontal axis of symmetry do not exist. Nevertheless, as described above, the seismic signal generated by these types of complexities theoretically has a distinctive signature. Therefore, we can to some extent filter it out and conserve only certain part of the purely anisotropic signal ( $\pi$  periodic with respect to the back azimuth). This way, our modeling effort can be focused on the information about seismic

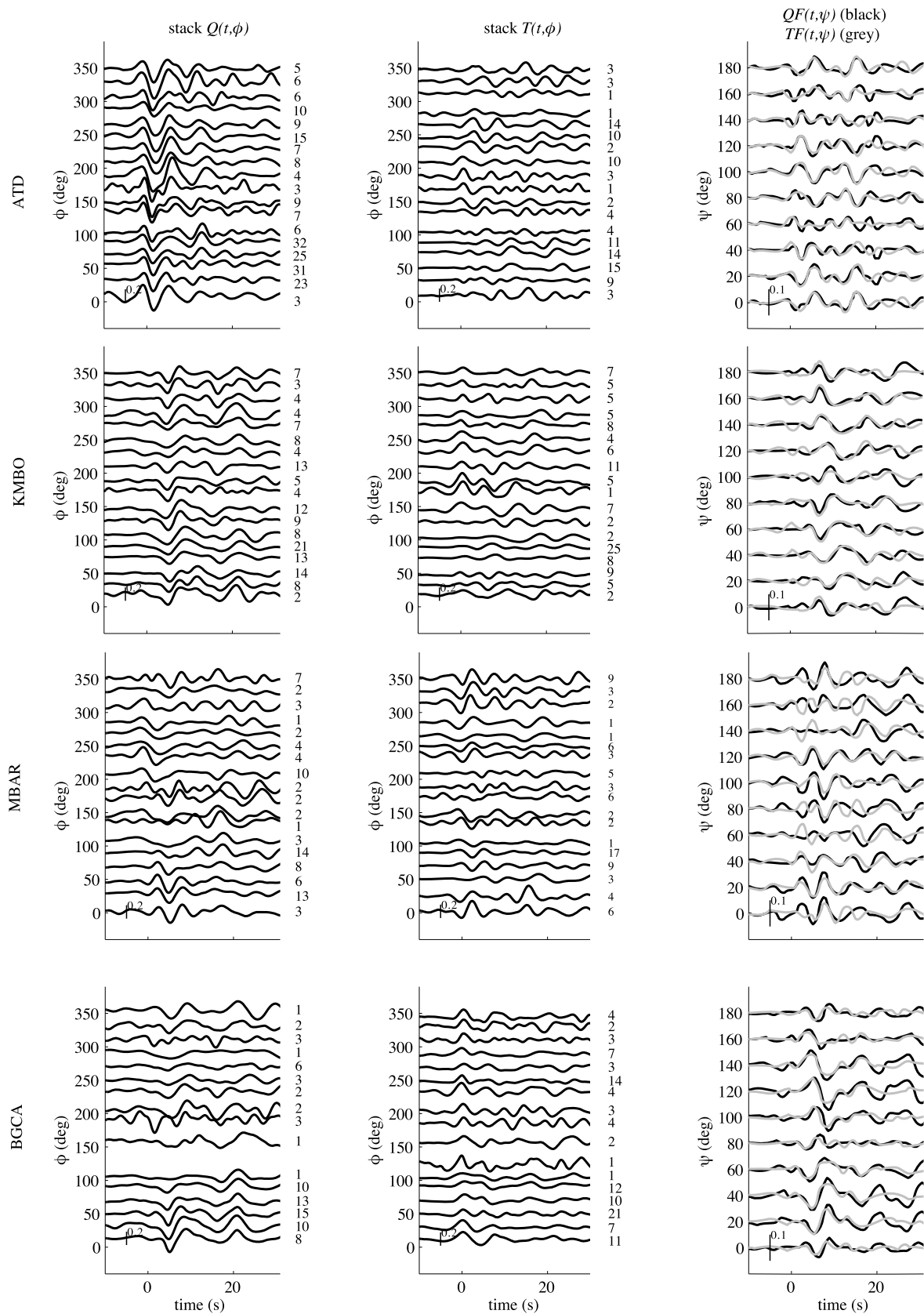


**Figure 3.** Stacks of receiver functions for each station. (left) Stacks of the Q (SV) components  $Q(t, \phi)$ , (middle) stacks of the T (SV) components  $T(t, \phi)$  and (right) signals  $QF(t, \psi)$  and  $TF(t, \psi)$  obtained by azimuthal filtering of the observed Q and T components, respectively;  $\phi$  and  $\psi$  stand for back azimuth. The number of individual RF in each stack is indicated on the right side of the corresponding plots.

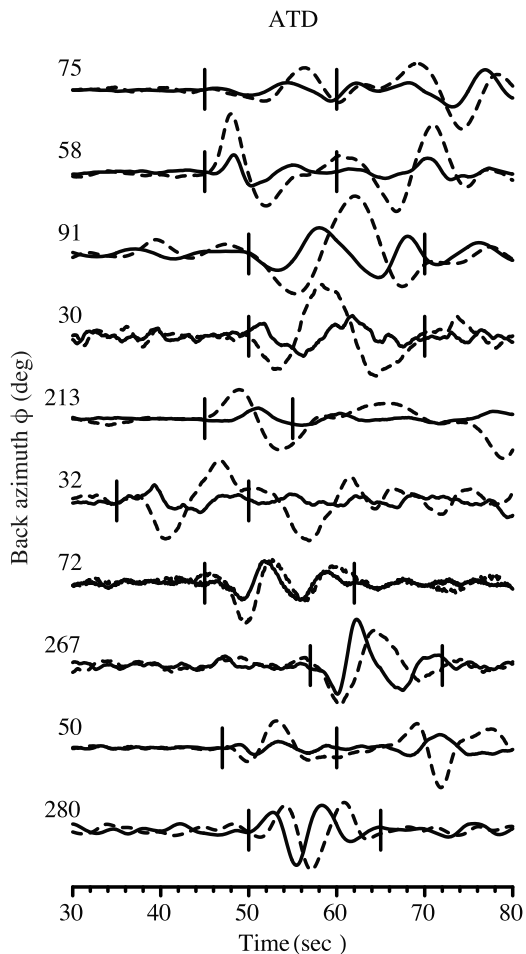


**Figure 4.** Observations of SKS splitting at station ATD. The dashed and solid lines are the radial and transverse signals, respectively. The number to the left of each plot is the back azimuth of the events.

anisotropy only. Note that by modeling the second azimuthal harmonic ( $\pi$  periodic), the information about the possible dip of the symmetry axis is lost. Assuming that the  $Q_i(t)$  and  $T_i(t)$  components of the individual RF are obtained for discrete values  $\phi_i$  of the back azimuth, we extract the second harmonics  $QF(t, \psi)$  and  $TF(t, \psi)$  of the Fourier series at back azimuth  $\psi$  by performing an azimuthally weighted summation:

$$QF(t, \psi) = \sum_i W_i^Q(\psi) Q_i(t)$$

$$TF(t, \psi) = \sum_i W_i^T(\psi) T_i(t)$$

with the weights

$$W_i^Q(\psi) = -\cos 2(\psi - \phi_i) / \sum_i \cos^2 2(\psi - \phi_i)$$

$$W_i^T(\psi) = \sin 2(\psi - \phi_i) / \sum_i \sin^2 2(\psi - \phi_i)$$

[9] If the medium is actually anisotropic,  $QF(t, \psi)$  and  $TF(t, \psi)$  should be similar in shape. Therefore, for inversion purpose, we directly use the average function  $SF(t, \psi) =$

$(QF(t, \psi) + TF(t, \psi))/2$ . We use only the first 25s after the direct P wave where the diagnostic of anisotropy is good. This part of the signal provides constraints on the anisotropic structure to a depth of roughly 200 km.

## 2.2. Shear Wave Splitting Observations

[10] SKS and SKKS waves are recorded at epicentral distances ranging from  $85^\circ$  to  $130^\circ$  and are filtered in the same manner as RF. The SKS and SKKS arrivals are then projected on the radial (R) and T directions. As described in section 2.1, anomalous transverse signal (Figure 4) in core refracted shear waves generally constitutes a reliable diagnostic of receiver side anisotropy.

## 2.3. Joint Inversion of the RF and SKS/SKKS Data Sets

[11] To perform the joint inversion, synthetic receiver functions and also SKS/SKKS synthetic waves are calculated and fitted to the real RF and SKS/SKKS data. The number of layers in the final model and their characteristics are conditioned by the waveforms of the data. The number of discontinuities in the vertical velocity profile directly controls the number of P-to-S converted phases observed in the P coda. The depth of these discontinuities (and the  $V_p/V_s$  ratio) determines the arrival time of the converted phases relative to the direct P wave. Finally, the nonzero transverse signal caused by the presence of anisotropy in a given layer exhibits azimuthal variations, the characteristics of which are controlled by the anisotropic properties, chiefly the percentage of anisotropy and the azimuth of the fast axis [Keith and Crampin, 1977; Savage, 1998; Levin and Park, 1998]. The seismologist who runs the inversion code chooses the final number of layers. Before starting the inversion, a trial number of layers is fixed. When this number is too small to take into account the complexity of the medium, the synthetic waveforms do not resemble the real ones. The number of layers is therefore increased and the inversion is run again. The number of layers is increased iteratively as long as it improves the fit to the data. When the number of layers becomes too large, the inversion does not converge to a satisfying new model. It means that the final model has parameters that exhibit substantial dispersion, or that the fit to the data becomes extremely poor. The final model may also strongly depend on the starting model. Finally, at certain point, adding extra layers may no longer modify the model substantially; that is, two layers have almost the same characteristics and could be merged without changing the general structure of the model (see Figure 6 and the auxiliary material).<sup>1</sup> All the issues mentioned above are used as hints by the seismologist who runs the code to decide that no more layers are needed.

[12] For each trial model  $m$ , the synthetic  $Q$  and  $T$  components of the receiver function are calculated by using the observed  $L_{obs}$  component:

$$Q_{syn}(t, m, c) = \frac{1}{2\pi} \int_{-\infty}^{\infty} \frac{H_Q(\omega, m, c)}{H_L(\omega, m, c)} L_{obs}(\omega) \exp(i\omega t) d\omega$$

$$T_{syn}(t, m, c) = \frac{1}{2\pi} \int_{-\infty}^{\infty} \frac{H_T(\omega, m, c)}{H_L(\omega, m, c)} L_{obs}(\omega) \exp(i\omega t) d\omega$$

<sup>1</sup>Auxiliary materials are available in the HTML. doi:10.1029/2009JB006923.

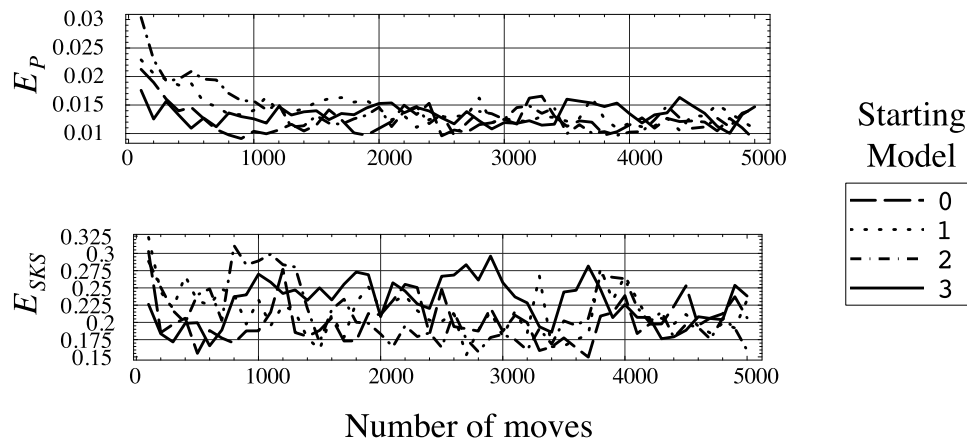


**Figure 5.** Evolution of the misfits  $E_P$  and  $E_{SKS}$  as functions of the number of moves for station ATD. The misfit functions are the RMS differences between the observed and synthetic receiver functions and SKS waveforms. (top) The misfit for the function  $SF(t, \psi) = \frac{1}{2}(QF(t, \psi) + TF(t, \psi))$ . (bottom) The T component of the SKS waves. Each plot (labeled 0 to 3) corresponds to a different starting model with randomly generated parameters (i.e., percentage of anisotropy, azimuth of the fast direction and thickness).

where  $\omega$  stands for angular frequency,  $m$  is the vector of the model parameters,  $c$  is apparent velocity and *obs* and *syn* refer to the observed RF and the synthetic one.  $H_Q$ ,  $H_T$  and  $H_L$  are theoretical transfer functions calculated using the Thomson-Haskell-Crampin algorithm [Keith and Crampin, 1977; Kosarev et al., 1979]. Assuming the crust and upper mantle can be modeled using an hexagonal symmetry with horizontal symmetry axis, the anisotropic stiffness tensor is fully described by five elastic parameters  $C$ ,  $A$ ,  $L$ ,  $N$ ,  $F$ . These parameters can be related to the isotropic and anisotropic components that describe the modeled medium using the following relations:

$$\sqrt{C/\rho} = V_p(1 + \delta V_p/2V_p)$$

$$\sqrt{A/\rho} = V_p(1 - \delta V_p/2V_p)$$

$$\sqrt{L/\rho} = V_s(1 + \delta V_s/V_s)$$

$$\sqrt{N/\rho} = V_s(1 - \delta V_s/V_s)$$

$$F = \eta(A - 2L)$$

$V_p$  and  $V_s$  are the mean (isotropic) compressional and shear velocities. We impose  $V_p/V_s = 1.8$  for sake of simplicity.  $\rho$  is the density and is calculated through the Birch formula  $\rho = 0.328V_p + 0.768$ .  $\delta V_p$  and  $\delta V_s$  are the difference between the  $V_p$  and  $V_s$  velocities parallel (fast) and perpendicular (slow) to the symmetry axis. The ratio between the percentage of anisotropy for the compressional and shear waves  $(\delta V_p/V_p)/(\delta V_s/V_s)$  is fixed at 1.5 based on the analysis of published data for the upper mantle [Oreshin et al., 2002]. The parameter  $\eta$  controls the velocity along the direction intermediate between the fast and the slow directions.  $\eta$  is fixed at 1.0 as in PREM [Dziewonski and Anderson, 1981].

[13] Theoretical T components of each SKS wave are calculated using their observed R component in the same way as described above to calculate synthetic Q and T receiver functions. The waveforms depend on the back azimuth (baz) from which a given SKS/SKKS wave comes.

[14] The inversion procedure consists of exploring the space of model parameters in order to minimize to misfit functions  $E_P(m)$  for the RF and  $E_{SKS}(m)$  for the SKS waves simultaneously. The misfit functions are the RMS differences between the synthetic and the observed RF/SKS. The search for the optimum model is achieved by using an approach similar to simulated annealing [Metropolis et al., 1953; Vestergaard and Mosegaard, 1991]. The misfit functions are minimized by iteratively disturbing the model parameters. Each move in the model space consists of perturbing a randomly selected single component of vector  $m$ . The perturbation is proportional to a random number, chosen uniformly between  $-1$  and  $1$ , and multiplied by the length between prior bounds. The value of the proportionality coefficient (equal to 0.1 as a rule) should be small enough to ensure correlation between the successive values of the cost functions [Tarantola, 2005]. The trial set of perturbations is accepted or rejected according to the Metropolis rule [Metropolis et al., 1953] which is used in cascade [Mosegaard and Tarantola, 1995] for the two misfit functions. This method does not require to sum the misfit functions and to choose weights. If  $m_c$  is the current model and  $m_a$  the attempted model, the later is accepted if it improves the model, i.e., if  $E_i(m_a) \leq E_i(m_c)$ , where  $i$  refers to P or SKS. If not, the attempted set of perturbations is accepted with probability  $\exp(E_i(m_c)/T_i - E_i(m_a)/T_i)$ , where  $T_i$  is temperature. Temperature schedule is an essential problem of a practical application of the *simulated annealing* techniques. We use a stepwise temperature function. For a given station, the search for the optimal model is achieved in several “steps,” each step corresponding practically to a full inversion (i.e., a program run). At each one of these steps, a constant value is assigned to the temperature. At each subsequent step, the assigned temperature value is smaller. As shown in Figure 5 of Vinnik et al. [2007], the final model parameters resulting from a full inversion will either exhibit high dispersion (their Figures 5a and 5b) or depend of the starting model (their Figures 5e and 5f) if the temperature is too high or too low, respectively. Trying several temperatures therefore allows us to choose the optimal one, i.e., the value that leads to the model with minimum dispersion on

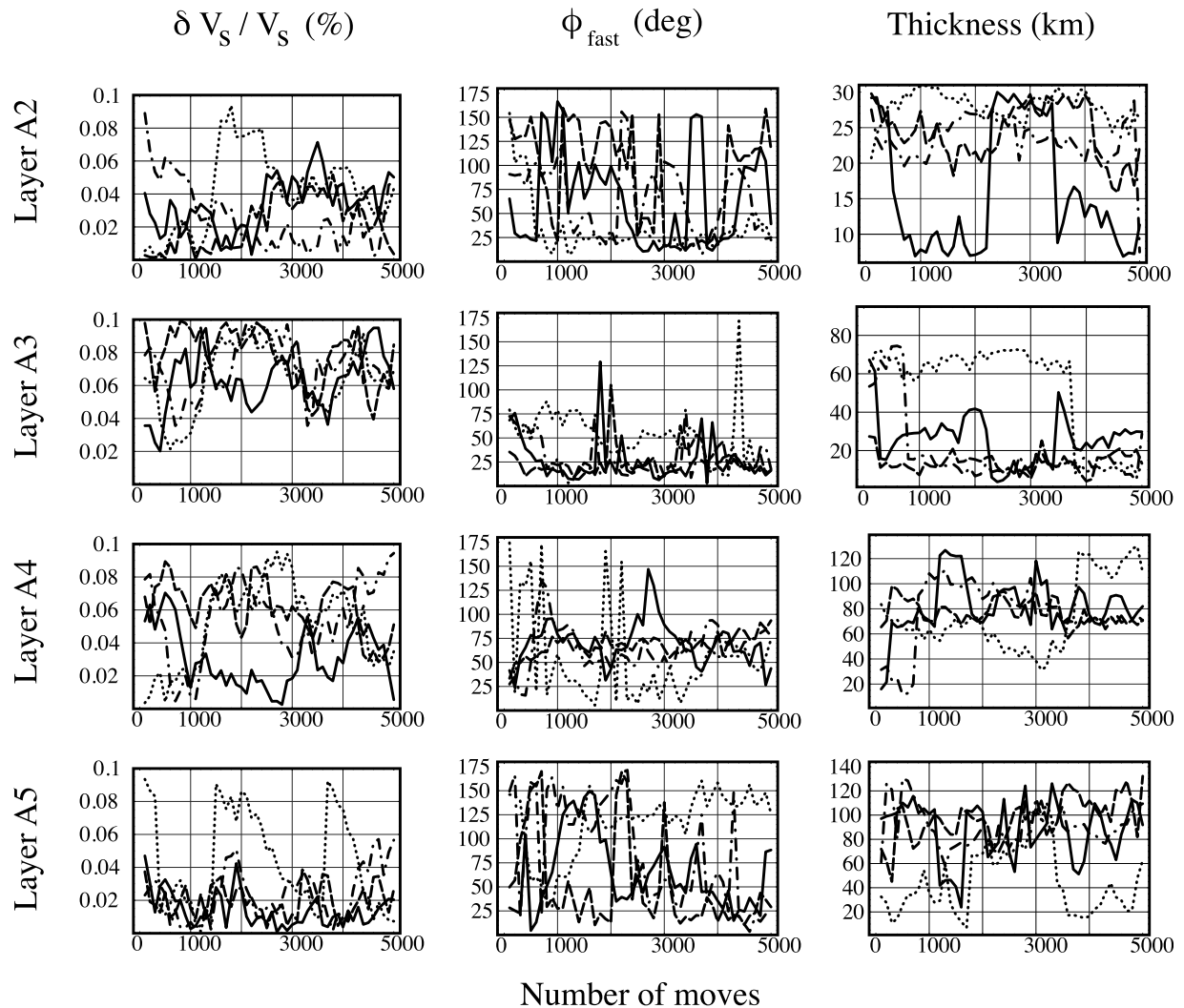


**Figure 6.** Evolution of the parameters of the model for station ATD as functions of the number of moves. Each color plot corresponds to a particular starting model as in Figure 5. (left) The percentage of anisotropy  $\delta V_s/V_s$ , (middle) the azimuth of the fast axis  $\phi_{fast}$ , and (right) the layer thickness.

parameters, on the one hand, and that does not depend on the starting model, on the other hand. Since we minimize two cost functions simultaneously ( $E_P$  and  $E_{SKS}$  for the receiver functions and SKS waveforms, respectively), we use two temperature functions  $T_P$  and  $T_{SKS}$ , which are adjusted independently. For a more detailed description of the inversion procedure including synthetic tests, see Vinnik *et al.* [2007].

[15] To illustrate the inversion procedure described above, the convergence of the model obtained for station ATD is depicted in Figures 5 and 6. For each run of the inversion, 4 randomly generated anisotropic models are used as starting models. Constraints from local isotropic models are used when available. In the case of ATD, we place a shallow low-velocity layer in the starting models since local models suggest it [Ayele *et al.*, 2004; Dugda *et al.*, 2005, 2007]. This first layer being quite thin, we do not try to resolve its possible anisotropic properties. The parameters of the three other layers, namely, their thickness (and thus the depth of the Moho discontinuity), percentage of anisotropy and the direction of the fast axis can evolve freely. The mean velocity

in each layer is imposed before inversion and is a simplified version of available model for the region (Dugda *et al.* [2007] in the case of ATD). As described above, during the inversion procedure, the exploration of the parameters space is guided by giving a probability to all the random perturbations that are iteratively imposed to the model. After 5000 iterations, the 2000 last models from each of the four series (i.e., the four starting models) are averaged after removing those that produce a bad fit. The resulting models for ATD are plotted in Figure 7 which depicts the number of hits in each cell of the parameter space. The final model (thick black dashed line) is the median of these models and the uncertainty on each individual parameter is defined as the standard deviation relative to this final model.

### 3. Results

[16] The good similarity of the Q and T components after azimuthal filtering is indicative of anisotropy (Figure 3). In addition, the anomalous transverse energy observed for a large number of the SKS arrivals (Figure 4) of our data set is

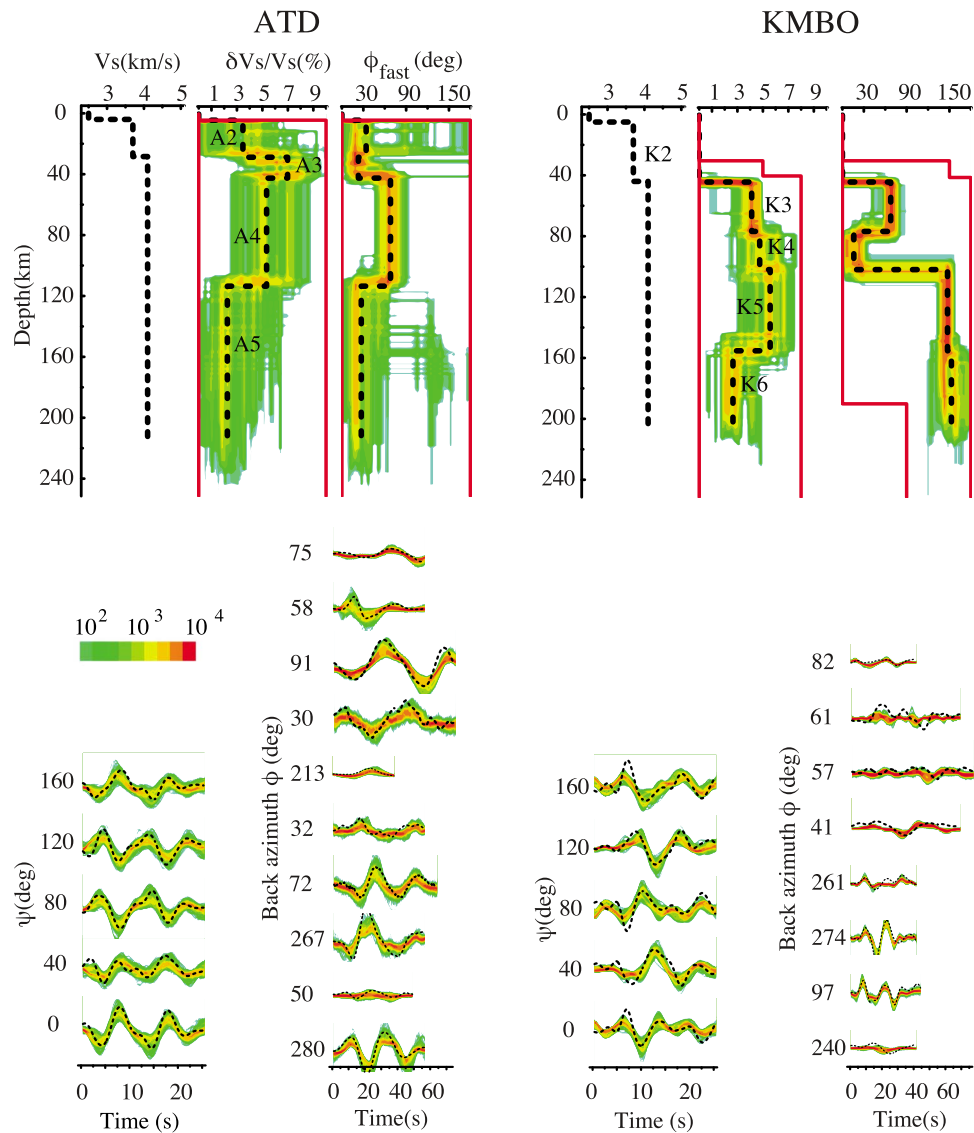


**Figure 7.** Depth-dependent anisotropic models for stations ATD and KMBO. (top) (left) The final S velocity profile. (middle and right) The selected models (the 2000 last models explored during the inversion search) as a function of the percentage of anisotropy and the direction of the fast axis. To visualize the results of the inversion, we divide the model space into cells and present the models by the number of hits in each cell. This number is shown using the color code described in the legend. The dashed line corresponds to the final model. The red solid lines bound the a priori search area in the model space. The misfits are shown beneath each model. (bottom) (left) Comparison of the observed (dashed lines) and synthetic (color) functions  $SF(t, \psi) = (QF(t, \psi) + TF(t, \psi))/2$ . (right) The misfit but for the T components of SKS waves. The layers are labeled to make it easier to identify them in the discussion.

also suggestive of the presence of anisotropy beneath all the stations used in this study.

[17] After running the inversion trying different numbers of layers, following the approach described in section 2, we find that the fit to the data at stations ATD, MBAR and KMBO is improved by using models with stratified anisotropy in the crust and/or upper mantle. The final models we obtained are described in Table 1 and shown in Figures 7 and 8. The parameters obtained display a wide range of values in terms of level of uncertainties. Individual layers with uncertainties on  $\phi_{fast}$  larger than  $35^\circ$  are not discussed. The rest is split into higher-quality (A) and lower-quality (B) layers. Layers

with uncertainties on the orientation of  $\phi_{fast}$  and on the thickness lower than  $15^\circ$  and 15 km, respectively, are ranked as A. Note that among the B-ranked layers, A3 and M4 exhibit uncertainties on  $\phi_{fast}$  close to the lower-quality threshold ( $32^\circ$  and  $30^\circ$ , respectively). As a comparison, we calculated synthetics RF and SKS waveforms using the model previously obtained for station ATD [Barruol and Hoffmann, 1999] based on SKS splitting observations only (Figure 9). This model contains a single layer of anisotropy and allows for a good fit of the SKS waveforms. Nevertheless, it does not satisfy the RF. The same test applied to the case of station KMBO and MBAR also shows that stratifi-

**Table 1.** Description of the Models<sup>a</sup>

Layer	Depth (km)	Thickness (km)	$V_s$ (km/s)	$\delta V_s/V_s$ (%)	$\phi_{fast}$ (deg)	Q
<i>ATD</i>						
A1	0–4	4(0)	2.5	0.0	-	-
A2	5–28	24(7)	3.7	3.5(1.7)	34(53)	-
A3	29–40	12(16)	4.1	7.0(1.5)	23(32)	B
A4	41–111	71(18)	4.1	5.3(1.6)	68(15)	B
A5	112–217	106(33)	4.1	2.2(1.7)	27(54)	-
<i>KMBO</i>						
K1	0–5	5(0)	2.5	0.0	-	-
K2	6–44	39(2)	3.7	0.0	-	-
K3	45–77	33(3)	4.1	4.1(0.7)	68(9)	A
K4	78–102	25(7)	4.1	4.8(1.2)	16(9)	A
K5	103–154	52(12)	4.1	5.6(1.1)	147(5)	A
K6	155–205	51(13)	4.1	2.6(0.9)	153(13)	A
<i>MBAR</i>						
M1	0–40	40(0)	3.5	0.0	-	-
M2	41–61	21(3)	4.1	7.6(1.0)	20(6)	A
M3	62–85	24(6)	4.1	4.9(2.0)	86(12)	A
M4	86–120	35(9)	4.1	3.9(1.5)	21(30)	B
M5 <sup>b</sup>	121–137	17(10)	4.1	3.0(2.2)	74(50)	-
M6 <sup>b</sup>	138–174	37(18)	4.1	3.5(2.4)	131(66)	-
<i>BGCA</i>						
B1	0–35	35(0)	3.5	0.0	-	-
B2	36–74	39(8)	4.5	6.9(1.7)	44(9)	A
B3 <sup>b</sup>	75–137	63(16)	4.5	1.4(1.3)	-	-
B4 <sup>b</sup>	138–196	59(24)	4.5	3.4(1.7)	137(34)	-

<sup>a</sup>For each individual layer,  $V_s$  is the mean shear velocity,  $\delta V_s/V_s$  is the percentage of anisotropy, and  $\phi_{fast}$  is the azimuth of the fast axis of propagation measured clockwise from north in degrees. For each parameter of the final models, the uncertainty is indicated in parentheses. Q is the quality rank assigned to each layer as described in section 3. Layers with uncertainties on  $\phi_{fast}$  larger than 35° are not considered robust and are not shown on Figure 1.

<sup>b</sup>For each station, we run the inversion using four different random starting models. Layers that do not appear in all four resulting models are considered as poorly constrained and are not shown in Figure 1.

cation is required to fit not only the SKS waveforms but also the RF (see auxiliary material).

[18] The model for ATD exhibits 2 B-ranked layers of anisotropy located in the upper mantle. The azimuth  $\phi_{fast}$  of the fast direction of anisotropy is NNE-SSW just beneath the Moho discontinuity (layers A3, Table 1). Then  $\phi_{fast}$  becomes ENE-WSW (layer A4, Table 1). The model for KMBO requires three main anisotropic layers all located in the upper mantle. The fast direction  $\phi_{fast}$  is oriented ENE-WSW from 45 to 77 km depth (layer K3), NNE-SSW from 78 to 102 km (layer K4) and NNW-SSE from 103–205 km (layers K5 and K6). For MBAR, the inversion produced two possible models (see Table 1 and auxiliary material). In both cases, from 41 to 61 km (layer M2) and then from 86 to roughly 120 km (layer M4),  $\phi_{fast}$  is NNE-SSW. Between these two layers,  $\phi_{fast}$  is E-W. The differences between the two final models for MBAR concern layers that are poorly resolved (M1 and M5–M6) and thus will not be discussed. For BGCA, the only robust feature (common to the four final models) is an anisotropic layer that extends from the Moho discontinuity to a depth of approximately 70 km (layer B2) and exhibits a roughly NE-SW fast direction (see Table 1 and auxiliary material).

## 4. Discussion

### 4.1. Possible Sources of Anisotropy

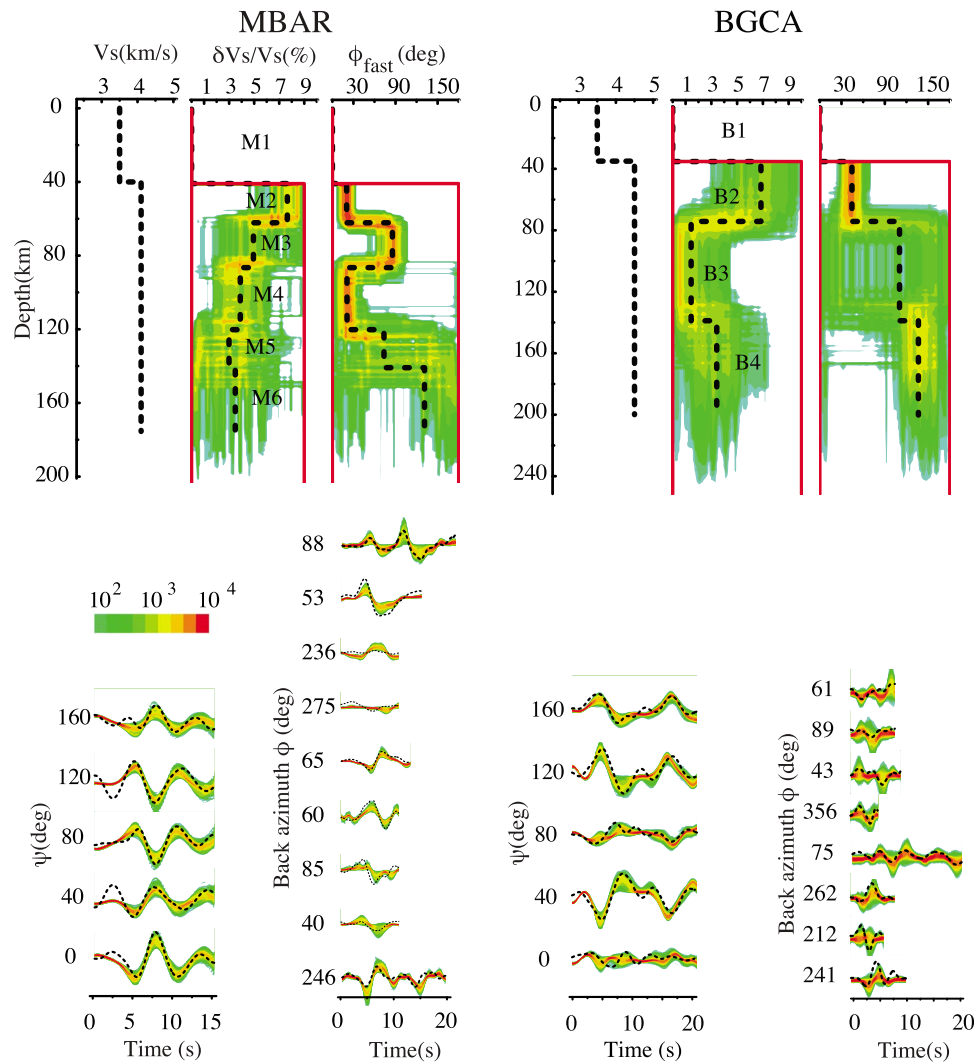
[19] Seismic anisotropy in the crust and upper mantle is thought to result mainly from the preferential alignment of

intrinsically anisotropic crystals or from that of fractures possibly filled with melt. The first case is referred to as lattice preferred orientation (LPO hereafter) and the second one as shape preferred orientation (SPO hereafter). Both crystal LPO and fracture/melt pocket SPO are governed to a large extent by the characteristic of the local tectonic setting.

[20] Laboratory experiments [Zhang and Karato, 1995; Jung and Karato, 2001] and numerical simulations [Ribe, 1992] show that under simple shear the fast  $a$  axis of olivine tends to become aligned parallel to the direction of maximum elongation producing bulk LPO anisotropy in upper mantle olivine aggregates. Where the lithosphere is tectonically heated such as along the EARS and in the Afar region, it becomes less rigid, and the reorientation of crystals is promoted. LPO-induced anisotropy has been used to explain several anisotropic patterns commonly observed over the globe and that may apply to our own case study. The fast direction of anisotropy that parallels the trend of several strike slip faults may result from anisotropic crystals LPO (such as olivine in the mantle and phyllosilicates in the crust) parallel to the plane of foliation [Levin et al., 2006; Vinnik et al., 2007]. Fossil olivine LPO left in the lithosphere during the most recent tectonic episode has also been invoked to explain anisotropy that correlates with the trend of major geological structures in regions of thick lithosphere [Silver, 1996]. Seismic anisotropy in some cases is also likely to result from asthenospheric flows. In areas where the fast axis of anisotropy correlates with the direction of the absolute plate motion (APM hereafter), the anisotropy may be induced by the shearing of the asthenospheric lid by the overriding plate [Vinnik et al., 1992; Hansen et al., 2006]. The asthenospheric flows and thus the associated LPO anisotropy may also be controlled by the topography of the base of the lithosphere. For instance, Walker et al. [2004] propose that the motion of the lithospheric root of the Tanzanian Craton leads the surrounding asthenosphere to be sheared and thus induces LPO anisotropy. Gradients in the topography of the lithosphere-asthenosphere boundary (LAB hereafter) can also cause mantle upwelling to be channeled. In particular, Hansen et al. [2006] and Montagner et al. [2007] found indications of asthenospheric flows channeled by the stretched lithosphere under the Red Sea and Aden Gulf, respectively.

[21] SPO anisotropy results from the closure of the fractures or melt pockets normal to the local direction of the maximum horizontal compressive stress (MHCS hereafter). The seismic waves with a polarization parallel to the opened fractures or melt pockets travel faster, yielding a fast direction of propagation parallel to the MHCS. Melt pocket SPO is more likely in region under hot, extensive setting such as rifts [Gao et al., 1997; Kendall et al., 2006].

[22] Due to the vertical variations of temperature and stress-strain state within the lithosphere and the asthenosphere, many of the anisotropic sources described above may coexist and contribute to the anisotropic signature observed in the RF and SKS splitting observations. In order to infer which of these possible sources is the dominant one at a given location and depth, we look for correlation between the fast direction of anisotropy in each layer and the trend of the several geotectonic features in East Africa, the estimates of the local APM and those for the MHCS. Note that the estimates of the APM depend on the model used (for example, NNR-NUVEL-1A versus HS3-NUVEL-1A as shown in



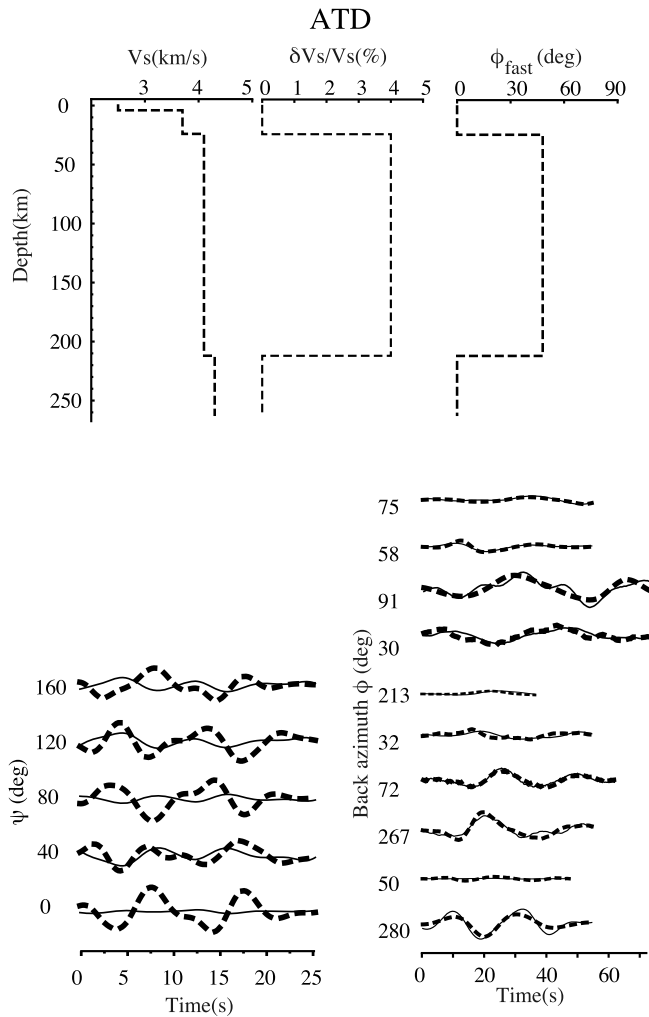
**Figure 8.** Same as Figure 7 but for MBAR and BGCA.

Figure 1) and that reliable estimates for the MHCS sometimes lack, especially around Afar (Figure 1).

#### 4.2. Effect From Lateral Heterogeneities and Dipping Structures

[23] As discussed in section 2, structural complexities common in real earth, chiefly lateral heterogeneities and dipping velocity structures, may be present beneath our set of stations and produce a signature in seismic signals that could be wrongly interpreted as an evidence of anisotropy. In the particular case of RF, as described before, extracting the second azimuthal harmonic allows isolating the purely anisotropic signature from that produced by small-scale random heterogeneities and dipping structures. The large-scale heterogeneities close to our stations (i.e., the boundaries of the EARS and that of the Tanzanian Craton) are far enough not to strongly overlap with the narrow Fresnel zones of the teleseismic body waves used in this study. Indeed, the anisotropic pattern in the vicinity of stations KMBO and ATD seems to be rather homogeneous, as indicated by the similarity of splitting observations between close stations around KMBO east from the flank of the eastern branch of the EARS

[Walker *et al.*, 2004] and also around ATD in the Afar depression [Hammond *et al.*, 2008]. The Moho structure is also rather flat in these two regions [Dugda *et al.*, 2005, 2007]. We can thus conclude that the signal we extract from SKS splitting and RF is dominated by anisotropy. In the case of MBAR, there is no close station with splitting observation and Moho depth estimate for comparison purpose. Nevertheless, MBAR is offset by a few tens of kilometers from the two closest structural discontinuities, namely, the flank of the western branch of the EARS and the limit of the Tanzanian Craton. The Moho is apparently flat in this region [Weeraratne *et al.*, 2003]. Using the argument of the narrow Fresnel zone, we can thus expect that the body waves recorded at MBAR are not dominantly affected by heterogeneities or dipping structures. Finally, in the case of BGCA, the presence of heterogeneities and its effect on SKS waveforms cannot be ruled out. Indeed, the splitting observations previously obtained at this station [Ayele *et al.*, 2004] slightly differs from those obtained for station BNG [Barruol and Hoffmann, 1999] that is located only a few tens of kilometers away from BGCA.



**Figure 9.** Single-layer anisotropic model for station ATD. The anisotropic parameters are  $\phi_{fast} = 43^\circ$  and  $\delta t = 1.6s$  and were taken from *Barruol and Hoffmann* [1999]. The delay time is converted to thickness supposing 4% of anisotropy.

### 4.3. Afar Area

[24] Beneath ATD, the NNE-SSW fast direction in the mantle layer A3 (29–40 km) is likely to be governed by LPO (Figure 10) induced by the local style of extension or by foliation. Indeed, the direction of  $\phi_{fast}$  is close to the NE-SW to NNE-SSW direction of tension inferred from earthquakes source mechanisms [see *Ayele et al.*, 2007, and references therein] and also close to the trend of the lateral shear zone along the western edge of the Ali Sabieh Block active since middle Miocene.  $\phi_{fast}$  in layers A3 does not seem to correlate with the trend of local MHCS and thus melt pockets SPO is not likely to be the dominant source of anisotropy there. Nevertheless, the presence of melt is highly probable in this region, as evidence by volcanism, and the absence of detectable anisotropy consistent with melt pockets SPO suggests the melt pockets either exhibit a spherical shape or are randomly oriented. Finally, we have to keep in mind that the uncertainty on  $\phi_{fast}$  is substantial for layer A3 ( $32^\circ$ ).

[25] The depth at which  $\phi_{fast}$  rotates from NNE-SSW (layers A3) to ENE-WSW (layer A4, 41–111 km) approx-

imatively coincides with the base of the lithospheric lid described in the model of *Dugda et al.* [2007]. Therefore, we interpret A4 as being asthenospheric in nature. In this layer,  $\phi_{fast}$  is not correlated with the MHCS either and SPO-induced anisotropy is unlikely. The ENE-WSW fast direction in A4 is parallel to the African APM in NNR-NUVEL-1A and could thus reflect APM-induced olivine LPO (Figure 1). Alternatively, the ENE-WSW fast direction in the asthenospheric layer A4 could represent an upwelling of hot material deflected and channeled by the thinned lithosphere beneath the Gulf of Aden. The idea of such a flow oriented from Afar to the Indian Ocean was proposed by *Montagner et al.* [2007] and is supported by radial anisotropy which is indicative of horizontal flow in the upper mantle beneath the Aden Gulf and also by Afar/Aden Gulf similar geochemical signatures [*Marty et al.*, 1996]. An aspect of our own model that is consistent with the channeled flow hypothesis is that the depth of the lower boundary of layer A4 (111 km) where  $\phi_{fast}$  no longer correlates with the trend of Gulf of Aden is close to that of the LAB away from the EARS and from the Aden Gulf in eastern Africa (100–125 km [*Juliá et al.*, 2005]) and in the Arabian shield (90 km [*Juliá et al.*, 2003; *Hansen et al.*, 2008]).

### 4.4. Stations on the Edges of the EARS

[26] Figure 11 describes our tentative model to explain the stratification of anisotropy beneath KMBO and MBAR. KMBO is located east from the Tanzanian Craton and from the eastern branch of the EARS (Figure 1). MBAR lies west from the Tanzanian Craton and east from the western branch of the EARS, on the Kibaran orogenic belt.

#### 4.4.1. Eastern Branch of the EARS

[27] Beneath station KMBO, the two uppermost anisotropic layers (K3, 45–77 km; K4, 78–102 km) seem to reflect two different structures located at the top and at the bottom of the mantle lithosphere, respectively. Indeed, estimates of the lithospheric thickness in this region ranges from  $\sim 90$  km [*Lew*, 2008] to  $\sim 105$  km [*Weeraratne et al.*, 2003]. In the upper half of the mantle lithosphere, the ENE-WSW fast direction (K3) aligns roughly normal to the trend of the Kenya rift, suggesting the anisotropy is governed by extension-induced LPO in the immediate vicinity of the rift. In the lower half of the mantle lithosphere, the NNE-SSW fast direction (K4) is in agreement with the trend of the local MHCS indicators (Figure 1) suggesting that SPO of melt inclusions controls the anisotropy. The asthenospheric temperature is probably anomalously high under this segment of the Kenyan rift as suggested by the low seismic velocities displayed in regional tomographic images [*Sebai et al.*, 2006; *Sicilia et al.*, 2008] and evidences for local extension accommodated by dike intrusions [*Calais et al.*, 2008]. Heating of the overlying lithosphere can promote the presence of melt pockets in layer K4 and enhance the reorientation of crystals normal to the rift in layer K3. Alternatively, the NNE-SSW fast direction of propagation in layer K4 that also parallels the trend of the Mozambique belt may reflect lithospheric frozen anisotropy associated with the orogenesis of this feature. Nevertheless, as just discussed, the presence of hot asthenosphere in this region raises doubt about the capacity of the deepest lithosphere to maintain a frozen fabric.

[28] The NNW-SSE fast axis of anisotropy in the asthenospheric layers K5 (103–154 km) and K6 (155–205 km) cor-

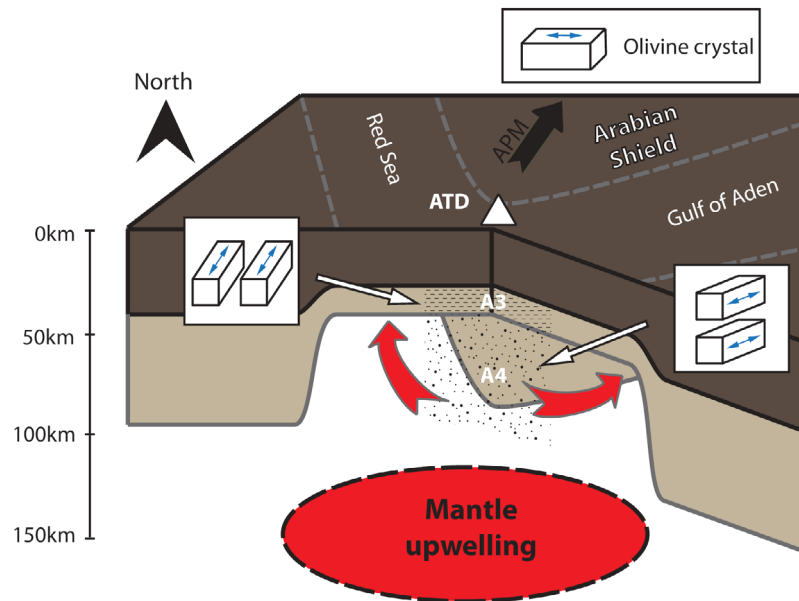


**Figure 10.** Tentative tectonic model to explain the stratification of anisotropy around Afar. The anisotropic layers are highlighted using distinctive textures. The elongated boxes represent olivine crystals with lattice preferred orientation (LPO). The blue arrows show the resulting fast axis of propagation. In the lithospheric layers A3 (29–40 km), the anisotropy is controlled by the local style of extension. The mobility of crust and mantle crystals is promoted by heating associated with the upwelling of slow (hot) mantle beneath the Afar Hot spot illustrated by red arrows. Where the lithosphere has been thinned through rift extension such as beneath the Gulf of Aden, the upwelling material is channeled (red arrows), explaining the ENE–WSW fast direction in layer A4 (41–111 km).

relates with the trend of the eastern edge of the Tanzanian Craton and thus could reflect asthenospheric flows around its lithospheric root [Walker *et al.*, 2004]. The percentage of anisotropy strongly drops at 154 km that roughly coincides to the estimated depth of the craton (around 170 km [Weeraratne *et al.*, 2003]). This is consistent with the idea of a flow guided by the keel of the craton that vanishes close to its bottom. The flow could result from the motion of Africa that induces shearing of the asthenosphere along the craton flanks. Alternatively, as mentioned before, regional tomographic studies suggest the presence of a large slow velocity anomaly that may be associated with upwelling. The mantle flow in this region could thus result from this hot mantle upwelling being deflected and guided by the stretched lithosphere beneath the eastern branch of the rift in a way similar to what Montagner *et al.* [2007] propose for the case of the Gulf of Aden.

#### 4.4.2. Western Branch of the EARS

[29] Beneath MBAR, the shallowest anisotropic layer (layer M2, 41–61 km) exhibits a fast axis parallel to the Kibaran belt which is potentially indicative of frozen lithospheric anisotropy related to the orogen of this feature. The anisotropic layer M3 (62–85 km) and layer M4 (86–120 km) display fast direction normal to the trend of the adjacent western branch of the EARS and parallel to the direction of the MHCS, respectively. We interpreted the anisotropic layers M3 and M4 as rift-normal extension-induced LPO in the middle part of the mantle lithosphere and melt pockets LPO just above the LAB, respectively. This pattern resembles that observed beneath KMBO on the opposite side of the Tanzanian craton, though layers K3 (45–77 km) and K4 (78–

102 km) lies deeper than M3 and M4. This observation is consistent with the tomographic model of Weeraratne *et al.* [2003], which indicates that around the Tanzanian Craton, the lithosphere is slightly thinner to the east than to the west. The area east from the Tanzanian Craton presumably lies over hot asthenosphere (see previous paragraph) whereas the region west of it lies above faster (cooler) asthenosphere. This contrast in the temperature state of the upper mantle may account for the difference in the lithospheric thickness (thermal erosion to the east). It also explains why the uppermost mantle lithosphere remains rigid enough to maintain frozen anisotropic fabric beneath MBAR (layer M2) but not beneath KMBO.

#### 4.5. Congo Craton

[30] The lithosphere beneath station BGCA located on the northern part of the Congo craton shows little anisotropy compared to the other stations of this study. The only well resolved anisotropic zone extends from the Moho discontinuity to a depth of 80 km. Our method does not allow to study the anisotropy of the asthenosphere in the case of BGCA since the lithospheric depth in this area ranges from 250 km [Risema and van Heijst, 2000] to more than 300 km [Begg *et al.*, 2009] which is deeper than the maximum depth of our models (see section 2.1). The absence of detectable anisotropy elsewhere than in layer B2 in the lithosphere may result from composite (incoherent) fabric acquired gradually during the large number of tectonic events that have shaped the Congo Craton over millions of years. Nevertheless, the model from Sicilia *et al.* [2008] suggests that the lithosphere is radially anisotropic from 60 km to at least 200 km close to

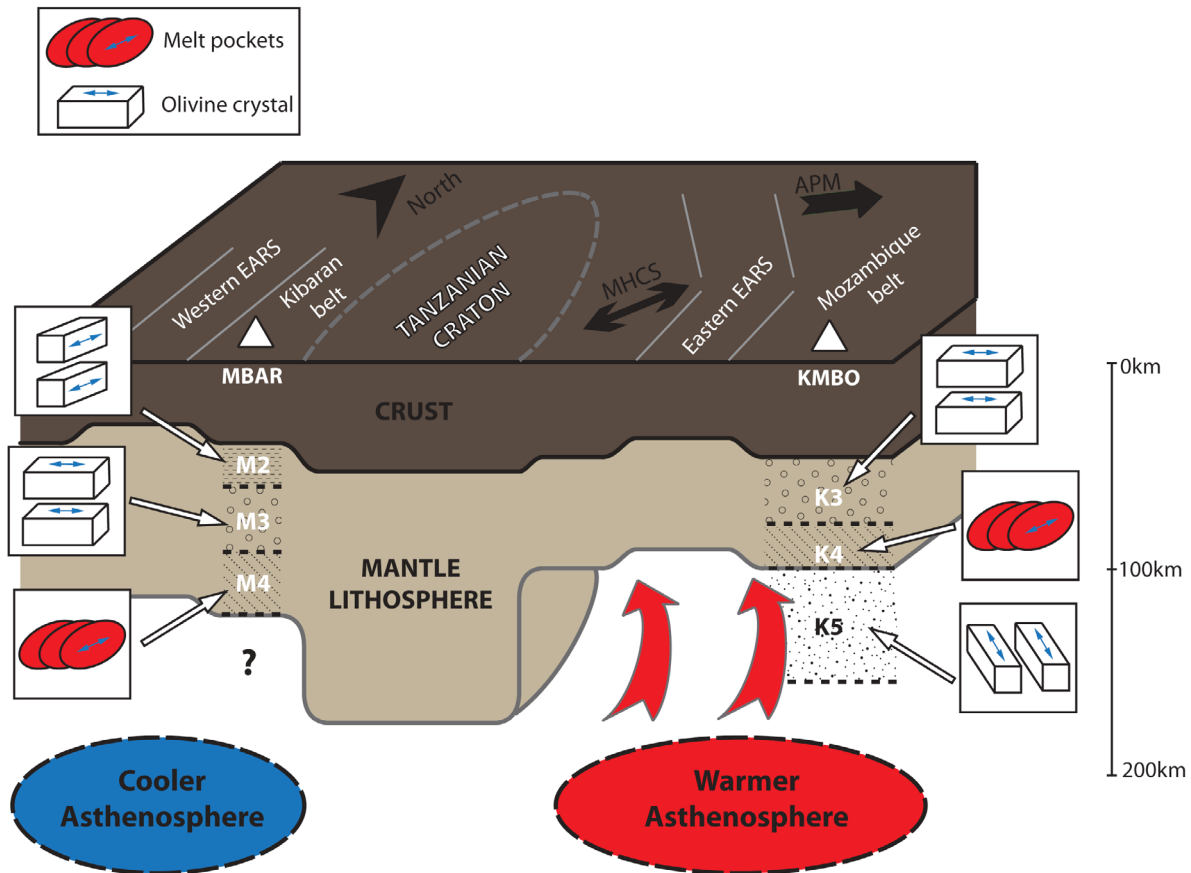


**Figure 11.** Tentative tectonic model to explain the stratification of anisotropy around the Tanzanian craton. Symbols are as in Figure 10. The red ellipses represent melt pockets that exhibit shape preferred orientation (SPO). Beneath MBAR, from the Moho discontinuity to the LAB, the source of anisotropy is fossil olivine LPO linked with the orogenesis of the Kibaran belt (M2), olivine LPO resulting from rift-normal extension (M3) and melt pocket SPO with preferential alignment close to the maximum horizontal compressive stress (M4). Beneath KMBO, the anisotropic source in the mantle lithosphere in K3 and K4 is the same as M3 and M4 beneath MBAR. In the asthenosphere, the anisotropic pattern in K5 results from flow around the lithospheric keel of the craton, induced either by the absolute motion of the African plate or by mantle upwelling locally guided by the topography of the base of the lithosphere. The LAB is shallower beneath KMBO than beneath MBAR, perhaps due to the warmer asthenosphere east from the Tanzanian Craton.

the site of BGCA. The fast direction of propagation in their model is vertical and thus would affect neither the SKS waves nor the P-to-S converted phases, remaining undetected using our method. This may explain the absence of anisotropy in our models below 80 km. The direction of  $\phi_{fast}$  seems correlated with the direction of the APM as indicated by model NNR-NUVEL-1A (though not by model HS3-NUVEL-1A) but layer B2 is too shallow to be affected by possible shearing at the LAB induced by the motion of the African continent. The direction of  $\phi_{fast}$  is not in agreement with the E-W direction of contraction inferred by *Ayele* [2002] either and thus is probably not controlled by the local stress field. BGCA is located close to an internal suture of the Congo Craton. We can speculate that the anisotropic fabric observed in our model is a relic of the strain pattern acquired during past continental assemblage. The shallow lithosphere is relatively stronger than the rest of the upper mantle and is then expected to remain undeformed between major tectonic episodes.

#### 4.6. Comparison With Previous Results From SKS Splitting Observations and Surface Waves

[31] In the models we obtained using joint inversion of RF and SKS splitting, stratification in seismic anisotropy is significant. This observation is in agreement with the models obtained all over the world using surface waves. For stations KMBO and MBAR, we found some agreement between the direction of anisotropy in the deep layers of our models and that of *Sicilia et al.* [2008] constrained using surface wave tomography. Aside from these cases, the overall agreement is poor. The sites of the stations we used in our study are often close to boundaries between regional anisotropic patterns associated with distinct tectonic provinces or structures. This is especially clear around stations ATD and MBAR where the model of *Sicilia et al.* [2008] displays very rapid changes. Owing to the poor lateral resolution of surface waves (around 500 km), at these particular points of the surface wave model, the retrieved fast direction represents

the smoothed transition between adjacent regional patterns rather than the real fast direction and cannot be reasonably compared with our models that benefit from a lateral resolution (up to 70 km) comparable to the scale of the fast variations in the anisotropic pattern.

[32] At stations MBAR and KMBO, the inconsistency between individual splitting measurements from distinct back azimuths previously reported [Barruol and Ben Ismail, 2001; Walker et al., 2004] is accounted for by using stratified models. This was previously demonstrated for station KMBO by Walker et al. [2004], who resolved a two-layer model from SKS splitting observations, though with no constraints on the depth of these layers. The anisotropic directions in layers K4 (78–102 km) and K5–K6 (103–205 km) of our model are similar to that retrieved by Walker et al. [2004]. By including constraints from RF we obtained information on the depth of the distinct layers and we detected an additional shallow layer (layer K3, 45–77 km). Our inversion requires the fast axis in layer K3 and that in layers K5–K6 to be orthogonal to each other. Under this configuration, part of the splitting accumulated in layers K5–K6 is canceled in layer K3 which may account for the large number of linear SKS phases reported earlier at station KMBO [Barruol and Ben Ismail, 2001; Walker et al., 2004]. The individual splitting observations at station MBAR are also inconsistent between each other and we similarly achieve reasonable fit of azimuthal variation of both the RF and the SKS splitting observations using a stratified model. For BGCA, our models display only one robust anisotropic layer where NE–SW fast direction slightly contrasts with the NNE–SSW direction obtained by Ayele et al. [2004]. We can speculate that this difference arises from anisotropic fabric at or beneath the LAB associated with the thick Congo Craton, i.e., deeper than the lower boundary of our model.

#### 4.7. Stratification of Seismic Anisotropy and Correlation With the Crust and Upper Mantle Discontinuities

[33] The vertical variations of the anisotropic properties in our models are apparently linked to a certain extent to the compositional and mechanical boundaries. On one hand, the layers that exhibit the highest percentage of anisotropy often lay immediately beneath the Moho discontinuity. This observation is true for most (ATD, MBAR, BGCA) but not all our models suggesting that it is not an artifact of the method. As illustrated by typical lithospheric strength envelopes [Kohlstedt et al., 1995], the uppermost mantle is commonly more resistant than the lower crust and the rest of the upper mantle that both behave in a ductile way. We would then intuitively expect the tectonic deformations and thus seismic anisotropy to concentrate in these weaker zones. In contrast to the direction of the fast axis which mainly depends on the mean orientation of the crystals, cracks or melt inclusions, the percentage of anisotropy is the combination of several factors such as rock composition and the portion of crystals or cracks effectively aligned in the mean fast axis direction. Therefore, we leave the interpretation concerning the generally higher percentage of anisotropy in the shallowest mantle lithosphere open for later investigation. On the other hand, the comparison of our models at ATD, KMBO and MBAR with detailed isotropic velocity models obtained from other studies seems to indicate that part of the vertical

discontinuities observed in the anisotropic properties are linked to the LAB. As revealed previously by several studies, the rigid lithosphere in stable areas tends to conserve the anisotropic fabric left by the last major tectonic episode [Silver, 1996; Fouch and Rondenay, 2006]. On the other hand, the anisotropy of the ductile asthenosphere and that of the lithosphere in area of active tectonism seem to be rather controlled by contemporaneous processes such as flow-induced crystal LPO [Vinnik et al., 1992; Zandt and Humphreys, 2008]. Our results follow this general rule. Stations MBAR, KMBO and ATD are located over area of intense tectonic activity and the anisotropy of both the lithosphere and asthenosphere seem to reflect mainly the current regional style of deformation. Thanks to the high vertical resolution of our approach, we found evidences that the lithosphere itself is stratified and reflects different sources of anisotropy. The vertical changes in the anisotropic properties seem to be controlled to some extent by differences in the thermal state of the mantle. As temperature increases, the lithosphere becomes ductile and loses its inherited fabric to acquire a new one, and eventually undergoes partial melting that generates anisotropy through melt pocket SPO. This is illustrated by our model for ATD, KMBO and MBAR described in Figures 10 and 11. At BGCA, we cannot look for correlation between the vertical anisotropic variations and the LAB due to the thick cratonic root. Nonetheless, the anisotropic layer we retrieved in the lithosphere shows no convincing correlations with any current tectonic process and may rather be linked to an inherited fabric from a remote tectonic episode, in agreement with what is generally observed in stable areas.

[34] **Acknowledgment.** S. Kiselev and L. Vinnik were supported by grant 10-05-00879 from the Russian Fund for Basic Research (RFBR).

#### References

- Ayele, A. (2002), Active compressional tectonics in central Africa and implications for plate tectonic models: Evidence from fault mechanism studies of the 1998 earthquakes in the Congo Basin, *J. Afr. Earth Sci.*, 35, 45–50, doi:10.1016/S0899-5362(02)00098-2.
- Ayele, A., G. W. Stuart, and J.-M. Kendall (2004), Insights into rifting from SKS splitting and receiver functions: an example from Ethiopia, *Geophys. J. Int.*, 157, 354–362, doi:10.1111/j.1365-246X.2004.02206.x.
- Ayele, A., G. Stuart, I. Bastow, and D. Keir (2007), The August 2002 earthquake sequence in north Afar: Insights into the neotectonics of the Danakil microplate, *J. Afr. Earth Sci.*, 48, 70–79, doi:10.1016/j.jafrearsci.2006.06.011.
- Barruol, G., and W. Ben Ismail (2001), Upper mantle anisotropy beneath the African IRIS and Geoscope stations, *Geophys. J. Int.*, 146, 549–561, doi:10.1046/j.0956-540x.2001.01481.x.
- Barruol, G., and R. Hoffmann (1999), Upper mantle anisotropy beneath Geoscope stations, *J. Geophys. Res.*, 104, 10,757–10,773, doi:10.1029/1999JB900033.
- Becker, T., S. Chevrot, V. Schulte-Pelkum, and D. Blackman (2006), Statistical properties of seismic anisotropy predicted by upper mantle geodynamic models, *J. Geophys. Res.*, 111, B08309, doi:10.1029/2005JB004095.
- Begg, G., et al. (2009), The lithospheric architecture of Africa: Seismic tomography, mantle petrology, and tectonic evolution, *Geosphere*, 5, 23–50, doi:10.1130/GES00179.1.
- Calais, E., et al. (2008), Strain accommodation by slow slip and dyking in a youthful continental rift, East Africa, *Nature*, 456, 783–787, doi:10.1038/nature07478.
- Debayle, E., J. J. Leveque, and M. Cara (2001), Seismic evidence for a deeply rooted low-velocity anomaly in the upper mantle beneath the northeastern Afro/Arabian continent, *Earth Planet. Sci. Lett.*, 193, 423–436, doi:10.1016/S0012-821X(01)00509-X.

- Dugda, M. T., A. A. Nyblade, J. Juliá, C. A. Langston, C. J. Ammon, and S. Simiyu (2005), Crustal structure in Ethiopia and Kenya from receiver function analysis: Implications for rift development in eastern Africa, *J. Geophys. Res.*, *110*, B01303, doi:10.1029/2004JB003065.
- Dugda, M. T., A. A. Nyblade, and J. Juliá (2007), Thin lithosphere beneath the Ethiopian Plateau revealed by a joint inversion of Rayleigh wave group velocities and receiver functions, *J. Geophys. Res.*, *112*, B08305, doi:10.1029/2006JB004918.
- Dziewonski, A. M., and D. L. Anderson (1981), Preliminary reference Earth model, *Phys. Earth Planet. Inter.*, *25*, 297–356, doi:10.1016/0031-9201(81)90046-7.
- Fouch, M. J., and S. Rondenay (2006), Seismic anisotropy beneath stable continental interiors, *Phys. Earth Planet. Inter.*, *158*, 292–320, doi:10.1016/j.pepi.2006.03.024.
- Gao, S., P. Davis, H. Liu, P. Slack, A. Rigor, Y. Zorin, V. Mordvinova, V. Kozhevnikov, and N. Logatchev (1997), SKS splitting beneath continental rift zones, *J. Geophys. Res.*, *102*(B10), 22,781–22,797, doi:10.1029/97JB01858.
- Girardin, N., and V. Farra (1998), Azimuthal anisotropy in the upper mantle from observations of P-to-S converted phases: Application to south-east Australia, *Geophys. J. Int.*, *133*(3), 615–629, doi:10.1046/j.1365-246X.1998.00525.x.
- Hammond, J. O., M. Guidarelli, M. Belachew, D. Keir, A. Ayele, C. Ebinger, G. Stuart, and J.-M. Kendall (2008), Seismic observations from the Afar Rift Dynamics Project: Preliminary results, *Eos Trans. AGU*, *89*(53), Fall Meet. Suppl., Abstract T43A-1980.
- Hansen, S., S. Schwartz, A. Al-Amri, and A. Rodgers (2006), Combined plate motion and density-driven flow in the asthenosphere beneath Saudi Arabia: Evidence from shear-wave splitting and seismic anisotropy, *Geology*, *34*(10), 869–872, doi:10.1130/G22713.1.
- Hansen, S., J. B. Gaherty, S. Y. Schwartz, A. Rodgers, and A. Al-Amri (2008), Seismic velocity structure and depth-dependence of anisotropy in the Red Sea and Arabian shield from surface wave analysis, *J. Geophys. Res.*, *113*, B10307, doi:10.1029/2007JB005335.
- Heidbach, O., M. Tingay, A. Barth, J. Reinecker, D. Kurfel, and B. Müller (2008), The 2008 release of the World Stress Map, Helmholtz Centre, Potsdam, Germany. (Available at <http://www.world-stress-map.org>)
- Juliá, J., C. J. Ammon, and R. B. Herrmann (2003), Lithospheric structure of the Arabian Shield from the joint inversion of receiver functions and surface-wave group velocities, *Tectonophysics*, *371*, 1–21, doi:10.1016/S0040-1951(03)00196-3.
- Juliá, J., C. J. Ammon, and A. A. Nyblade (2005), Evidence for mafic lower crust in Tanzania, East Africa, from joint inversion of receiver functions and Rayleigh wave dispersion velocities, *Geophys. J. Int.*, *162*, 555–569, doi:10.1111/j.1365-246X.2005.02685.x.
- Jung, H., and S.-I. Karato (2001), Water-induced fabric transitions in olivine, *Science*, *293*, 1460–1463, doi:10.1126/science.1062235.
- Keith, C. M., and S. Crampin (1977), Seismic body waves in anisotropic media: reflection and refraction at a plane interface, *Geophys. J. R. Astron. Soc.*, *49*, 181–208.
- Kendall, J.-M., S. Piliidou, D. Keir, I. Bastow, G. Stuart, and A. Ayele (2006), Mantle upwellings, melt migration and magma assisted rifting in Africa: Insights from seismic anisotropy, in *Structure and Evolution of the Rift Systems Within the Afar Volcanic Province, Northeast Africa*, edited by G. Yirgu, C. J. Ebinger, and P. K. H. Maguire, *Geol. Soc. Spec. Publ.*, *259*, 57–74.
- Kohlstedt, D. L., B. Evans, and S. J. Mackwell (1995), Strength of the lithosphere: Constraints imposed by laboratory experiments, *J. Geophys. Res.*, *100*, 17,587–17,602, doi:10.1029/95JB01460.
- Kosarev, G. L., L. I. Makeyeva, E. F. Savarensky, and E. M. Chesnokov (1979), Influence of anisotropy beneath seismograph station on body waves, *Fiz. Zemli*, *2*, 26–37.
- Levin, V., and J. Park (1998), P-SH conversions in layered media with hexagonally symmetric anisotropy: A cookbook, *Pure Appl. Geophys.*, *151*, 669–697, doi:10.1007/s000240050136.
- Levin, V., A. Henza, J. Park, and A. Rodgers (2006), Texture of mantle lithosphere along the Dead Sea Rift: Recently imposed or inherited?, *Phys. Earth Planet. Inter.*, *158*, 174–189, doi:10.1016/j.pepi.2006.05.007.
- Lew, K. (2008), The lithosphere-asthenosphere boundary beneath the Tanzanian Craton, *Eos Trans. AGU*, *89*(53), Fall Meet. Suppl., Abstract s31-1880.
- Marty, B., R. Pik, and G. Yirgu (1996), Helium isotopic variations in Ethiopian plume lavas: Nature of magmatic sources and limit on lower mantle contribution, *Earth Planet. Sci. Lett.*, *144*, 223–237, doi:10.1016/0012-821X(96)00158-6.
- Metropolis, N., M. Rosenbluth, A. Rosenbluth, A. Teller, and E. Teller (1953), Equation of state calculations by fast computing machines, *J. Chem. Phys.*, *21*, 1087–1092, doi:10.1063/1.1699114.
- Montagner, J. P., et al. (2007), Mantle upwellings and convective instabilities revealed by seismic tomography and helium isotope geochemistry beneath eastern Africa, *Geophys. Res. Lett.*, *34*, L21303, doi:10.1029/2007GL031098.
- Mosegaard, K., and A. Tarantola (1995), Monte carlo sampling of solutions to inverse problems, *J. Geophys. Res.*, *100*, 12,431–12,447, doi:10.1029/94JB03097.
- Oreshin, S., L. Vinnik, Makeyeva, G. Kosarev, R. Kind, and F. Wenzel (2002), Combined analysis of SKS splitting and regional P traveltimes in Siberia, *Geophys. J. Int.*, *151*, 393–402, doi:10.1046/j.1365-246X.2002.01791.x.
- Ribe, N. M. (1992), On the relation between seismic anisotropy and finite strain, *J. Geophys. Res.*, *97*, 8737–8747, doi:10.1029/92JB00551.
- Ritsema, J., and H. van Heijst (2000), New seismic model of the upper mantle beneath Africa, *Geology*, *28*(1), 63–66, doi:10.1130/0091-7613(2000)28<63:NSMOTU>2.0.CO;2.
- Ritsema, J., H. J. van Heijst, and J. H. Woodhouse (1999), Complex shear wave velocity structure imaged beneath Africa and Iceland, *Science*, *286*, 1925–1928, doi:10.1126/science.286.5446.1925.
- Savage, M. (1998), Lower crustal anisotropy or dipping boundaries? Effects on receiver functions and a case study in New Zealand, *J. Geophys. Res.*, *103*, 15,069–15,087, doi:10.1029/98JB00795.
- Savage, M. K. (1999), Seismic anisotropy and mantle deformation: What have we learned from shear wave splitting?, *Rev. Geophys.*, *37*, 65–106, doi:10.1029/98RG02075.
- Sebai, A., E. Stutzmann, J. P. Montagner, E. Beucler, and D. Sicilia (2006), Upper mantle anisotropic structure beneath Africa, *Phys. Earth Planet. Inter.*, *155*, 48–62, doi:10.1016/j.pepi.2005.09.009.
- Sicilia, D., et al. (2008), Shear-wave velocities and stratification of anisotropic upper mantle structure beneath the Afar Hotspot region, *Tectonophysics*, *462*, 164–177, doi:10.1016/j.tecto.2008.02.016.
- Silver, P. G. (1996), Seismic anisotropy beneath the continents: probing the depths of geology, *Annu. Rev. Earth Planet. Sci.*, *24*, 385–432, doi:10.1146/annurev.earth.24.1.385.
- Tarantola, A. (2005), Inverse Problem Theory and Methods for Model Parameter Estimation, Soc. for Ind. and Appl. Math., Philadelphia, Pa.
- Vestergaard, P. D., and K. Mosegaard (1991), Inversion of post-stack seismic data using simulated annealing, *Geophys. Prospect.*, *39*, 613–624, doi:10.1111/j.1365-2478.1991.tb00332.x.
- Vinnik, L. (1977), Detection of waves converted from P to SV in the mantle, *Phys. Earth Planet. Inter.*, *15*, 39–45, doi:10.1016/0031-9201(77)90008-5.
- Vinnik, L., and J. P. Montagner (1996), Shear-wave splitting in the mantle Ps phases, *Geophys. Res. Lett.*, *23*, 2449–2452, doi:10.1029/96GL02263.
- Vinnik, L. P., L. I. Makeyeva, A. Milev, and A. Y. Usenko (1992), Global patterns of azimuthal anisotropy and deformations in the continental mantle, *Geophys. J. Int.*, *111*(3), 433–447, doi:10.1111/j.1365-246X.1992.tb02102.x.
- Vinnik, L. P., I. M. Aleshin, S. G. Kiselev, G. L. Kosarev, and L. I. Makeyeva (2007), Depth localized azimuthal anisotropy from SKS and P receiver functions: The Tien Shan, *Geophys. J. Int.*, *169*, 1289–1299, doi:10.1111/j.1365-246X.2007.03394.x.
- Walker, K. T., A. A. Nyblade, S. L. Klemperer, G. H. R. Bokelmann, and T. J. Owens (2004), On the relationship between extension and anisotropy: Constraints from shear wave splitting across the East African Plateau, *J. Geophys. Res.*, *109*, B08302, doi:10.1029/2003JB002866.
- Weeraratne, D. S., D. W. Forsyth, K. M. Fischer, and A. A. Nyblade (2003), Evidence for an upper mantle plume beneath the Tanzanian craton from Rayleigh wave tomography, *J. Geophys. Res.*, *108*(B9), 2427, doi:10.1029/2002JB002273.
- Zandt, G., and E. Humphreys (2008), Toroidal mantle flow through the western U.S. slab window, *Geology*, *36*(4), 295–298, doi:10.1130/G24611A.1.
- Zhang, S., and S. I. Karato (1995), Lattice preferred orientation of olivine aggregates deformed in simple shear, *Nature*, *375*, 774–777, doi:10.1038/375774a0.

S. Kiselev and L. Vinnik, Institute of physics of the Earth, B. Grouzinskaya 10, 123995 Moscow, Russia. (kiselev@ifz.ru; vinnik@ifz.ru)

J.-P. Montagner, Département de Sismologie, Institut de Physique du Globe de Paris, 4, pl. Jussieu, Case 89, F-75252 Paris CEDEX 05, France. (jpm@igpp.jussieu.fr)

M. Obrebski, Seismological Laboratory, Earth and Planetary Science, University of California, Berkeley, 215 McCone Hall 4760, Berkeley, CA 94720-4760, USA. (obrebski@berkeley.edu)